ELSEVIER

Physica D 131 (1999) 78–89

PHYSICA D

Quantum chaos with cesium atoms: pushing the boundaries

B.G. Klappauf, W.H. Oskay, D.A. Steck, M.G. Raizen *

Department of Physics, The University of Texas at Austin, Austin, TX 78712-1081, USA

Abstract

Atomic motion in pulsed, periodic optical potentials provides a unique experimental testing ground for quantum chaos. In the first generation of experiments with sodium atoms we observed dynamical localization, a quantum suppression of chaotic diffusion. To go beyond this work we have constructed an experiment with cold cesium atoms, and report our first results from this system. The larger mass and longer wavelength push out the momentum boundary in phase space that arises from the nonzero duration of the pulses. This feature should enable the study of noise effects and dimensionality on dynamical localization. We propose a new method of quantum state preparation based on stimulated Raman transitions for studies of mixed phase space dynamics.

PACS: 05.45.+b, 32.80.Pj, 42.50.Vk, 72.15.Rn
Keywords: Kicked rotor; Quantum chaos; Dynamical localization; Atom optics

1. Introduction

The interface between nonlinear dynamics and quantum mechanics has become an active area of research in recent years. One of the key results in this field, due to Boris Chirikov and co-workers, is dynamical localization. This striking effect is a quantum suppression of classical (chaotic) diffusion, and has stimulated a great deal of interest and discussion since it was first predicted almost 20 years ago [1–9].

Rydberg atoms in strong microwave fields provided the first experimental system that addressed this problem, and the observed suppression of ionization was attributed to dynamical localization [10–13]. To go beyond these results, it is important to find new experimental systems to investigate dynamical localization as well as other problems in quantum chaos.

In general, the observation of dynamical localization requires a predominantly chaotic (classical) phase space, because diffusion can be restricted by residual stable islands and by classical boundaries according to the Kolmogorov, Arnol'd, Moser (KAM) theorem [14]. In addition, the duration of the experiment must exceed the "quantum break time", when quantum effects manifest themselves. Finally, the system must be sufficiently isolated from the environment that quantum interference effects can persist. All of these conditions can be satisfied by a system of cold atoms that are exposed to time-dependent standing waves of light [15,16]. The typical potentials in this system are highly nonlinear, resulting in chaotic classical dynamics. Since dissipation can be made negligibly small in this system, quantum effects can become important. These features led to a series of experiments in our

* Corresponding author. E-mail: raizen@physics.utexas.edu.

0167-2789/99/$ – see front matter
PII: S0167-2789(98)00221-8

group on dynamical localization and quantum chaos with cold sodium atoms, establishing atom optics as a new experimental testing ground for the field [17–21]. The simplest experimental configuration in that work was a standing wave of light that was pulsed on periodically. This system was an experimental realization of the kicked rotor, which has been a paradigm for classical and quantum chaos for many years.

To go beyond this first generation of experiments, we wish to address several key topics. The first is to study the effects of noise and dissipation on dynamical localization. The signature in this case is the destruction of localization, with subsequent diffusive growth in momentum [22–24]. A second direction is to study the role of dimensionality on dynamical localization. While exponential localization occurs in one dimension, a sharp increase in the width of the exponentially localized momentum distributions is predicted in two dimensions, and a transition to a delocalized state is predicted in three dimensions [25].

Early efforts to observe these effects in sodium were hampered by the presence of a boundary in momentum space that arises from the nonzero pulse duration of the interaction Hamiltonian [19]. To overcome this problem, we have constructed a new experiment with laser-cooled cesium atoms. The larger atomic mass and the longer wavelength of the atomic transition push out the boundary to much higher momenta.

This paper describes our new cesium experiment, which is a realization of the quantum kicked rotor, and presents a detailed study of boundary effects on dynamical localization. In Section 2 we give a theoretical background on atomic motion in a far-detuned dipole potential, and provide a classical analysis of the boundary in phase space. In Section 3 we describe the general experimental approach. In Section 4 we discuss the new experimental results with cesium. Finally, in Section 5 we describe some directions for future work including a new method of quantum state preparation based on stimulated Raman transitions. This method will prepare an initial condition that is a minimum uncertainty state in phase space, opening the way for detailed studies of quantum transport in mixed phase space.

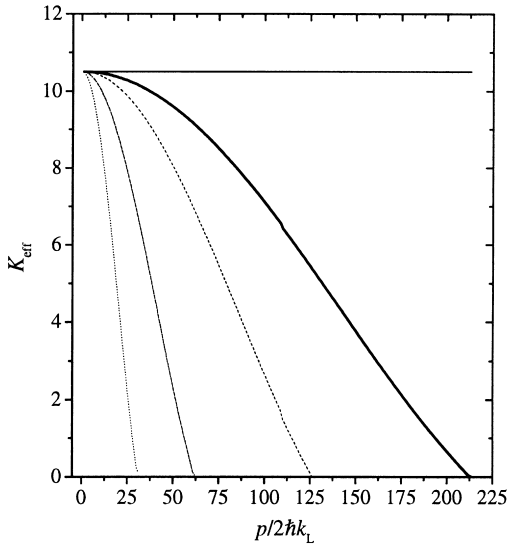

Fig. 1. Classical calculation of the effective stochasticity parameter K_{eff} as a function of momentum for square pulses of various temporal widths. The horizontal line represents the δ-kick case. The other curves represent square pulses with widths $\alpha = 0.014$ (heavy solid line), $\alpha = 0.024$ (dashed), $\alpha = 0.049$ (dash–dot), and $\alpha = 0.099$ (dotted). The well depth is adjusted in each case to give the same maximum value of $K_{\text{eff}} = 10.5$ at $p/2\hbar k_{\text{L}} = 0$. The point where K_{eff} drops to ~ 1 in each case is the classical momentum boundary. The typical limit of our momentum measurements is $|p/2\hbar k_{\text{L}}| \approx 80$. Note that we have suppressed the curves after their first zero-crossing.

2. Theoretical background

To describe our system we begin with a two-level atom with transition frequency ω_0 interacting with a pulsed standing wave of linearly polarized, near-resonant light of frequency ω_{L}. For sufficiently large detuning $\delta_{\text{L}} = \omega_0 - \omega_{\text{L}}$ (relative to the natural linewidth), the excited state amplitude can be adiabatically eliminated [16]. The atom can then be treated as a point particle. This approximation leads to the following kicked-rotor Hamiltonian for the center-of-mass motion of the atom

$$H = p^2/2M + V_0 \cos(2k_{\text{L}}x) \sum_{n=-\infty}^{\infty} F(t - nT). \quad (1)$$

Here $V_0 = \hbar\Omega^2/8\delta_{\text{L}}$, k_{L} is the wave number of the light, $\Omega = 2\mu E_0/\hbar$ the resonant Rabi frequency, μ the atomic dipole moment, E_0 the electric field of a single traveling wave component of the standing

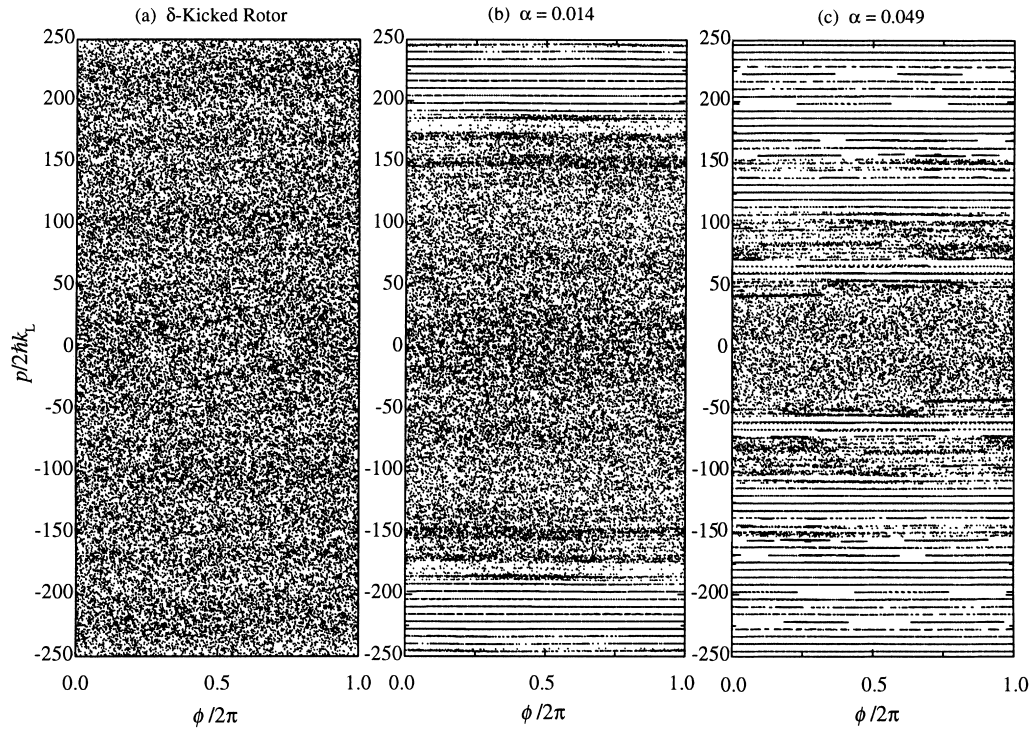

Fig. 2. Classical phase portraits for the kicked rotor with $K = 10.5$, comparing δ-kicks (a) to square pulses of widths $\alpha = 0.014$ (b) and $\alpha = 0.049$ (c). Case (b) is typical for our localization experiments. This case mimics the δ-kicked rotor for a momentum region much larger than that used in our experiments ($|p/2\hbar k_L| \lesssim 80$).

wave, $F(t)$ a pulse centered at $t = 0$ with duration t_p, and T is the period of the standing wave pulses. It is convenient to rescale our coordinates and use the dimensionless Hamiltonian

$$H = \rho^2/2 + k\cos(\phi)\sum_{n=-\infty}^{\infty} f(\tau - n), \tag{2}$$

where $\phi = 2k_L x$, $\rho = (2k_L T/M)p$, $\tau = t/T$, $f(\tau)$ is a pulse of unit amplitude and scaled duration $\alpha = t_p/T$, $k = (8V_0/\hbar)\omega_r T^2$ is the scaled kick amplitude, $\omega_r = \hbar k_L^2/2M$ is the recoil frequency, $H' = (4k_L^2 T^2/M)H$, and we have dropped the prime on H. In the quantized model, ϕ and ρ are conjugate variables that satisfy the commutation relation $[\phi, \rho] = i\bar{k}$, where $\bar{k} = 8\omega_r T$ is a scaled Planck constant. In the limit where $f(\tau)$ becomes a δ-function, the product ηk reduces to the classical stochasticity parameter K for the δ-kicked rotor, where $\eta = \int_{-\infty}^{\infty} f(\tau)\mathrm{d}\tau$. The stochasticity parameter completely specifies the classical δ-kicked rotor dynamics. For $K \gtrsim 1$ the classical δ-kicked rotor dynamics are globally chaotic, in the sense that there are no invariant tori that prevent trajectories in the main chaotic region from attaining arbitrarily large momenta. For $K > 4$ the primary resonances become unstable, and the phase space is predominantly chaotic.

The effects of a nonzero pulse width can be seen by rewriting the sequence of kicks as a discrete Fourier series and analyzing the amplitudes of the primary resonances of the system. Applying this procedure to the Hamiltonian (2)

$$H = \rho^2/2 + k\sum_{m=-\infty}^{\infty} \tilde{f}(2\pi m)\cos(\phi - 2\pi m\tau), \tag{3}$$

where $\tilde{f}(2\pi m)$ is the Fourier transform of the pulse function $f(\tau)$. This Hamiltonian has primary resonances located at $\rho = \mathrm{d}\phi/\mathrm{d}t = 2\pi m$. Therefore, the Fourier transform evaluated at $m = \rho/2\pi$ modifies the effective stochasticity parameter K_{eff} as a function of

momentum. For a square pulse, which approximates the pulse used in our experiments, this factor can be written as

$$K_{\text{eff}} = \alpha k \frac{\sin(\alpha\rho/2)}{\alpha\rho/2}, \tag{4}$$

where $K_{\text{eff}}(\rho = 0) = \alpha k$ plays the role of the δ-kicked rotor stochasticity parameter K. This dependence of K_{eff} on momentum is displayed in Fig. 1, which compares several square-pulse cases to the δ-kick case. The dynamics of the system undergo a transition as K_{eff} drops to ~ 1, because of the presence of KAM surfaces that span the phase space and act as a barrier against momentum diffusion. This *momentum boundary* is illustrated in Fig. 2, which shows classical phase portraits for the δ-kicked rotor (Fig. 2(a)) and two square-pulse cases (Figs. 2(b) and (c)). The phase portrait of Fig. 2(b) is typical of our current cesium experiment, and the boundaries are well outside the range of detectable atomic momenta, $|p/2\hbar k_{\text{L}}| \lesssim 80$. Our previous experimental work in sodium was limited to a bounded chaotic region similar to that in Fig. 2(c). While this situation enabled the observation of the transition from the short time classical diffusion to the exponential localization of the momentum distribution after the quantum break time, it could not be used to explore any continued momentum growth due to delocalization beyond that point.

Fig. 3 shows classical Monte-Carlo simulations (with 2×10^5 particles) of the same systems as in Fig. 2. The momentum distributions after 68 kicks are plotted here. The distributions are similar in the central region, but the boundary suppresses diffusion in the wings of the distributions in the square-pulse cases, especially in the case with the widest pulses ($\alpha = 0.049$). The nearly Gaussian initial momentum distribution is also plotted, and it corresponds to the initial distribution in the experiments.

A simple classical model of the boundary provides us with relevant scaling parameters and makes clear the advantage of using cesium rather than sodium. Consider an atom with a momentum such that it travels one period of the standing wave during a kick. Then the momentum transferred to the atom by the potential averages to zero, and the particle no longer diffuses.

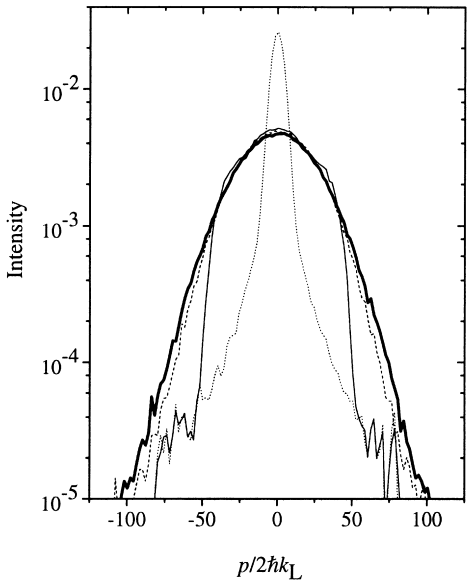

Fig. 3. Comparison of momentum distributions from classical simulations for different pulse widths after 68 kicks, with $K = 10.5$. The nearly Gaussian initial condition is shown as a dotted line. Notice that even for $\alpha = 0.014$ (dashed), the classical growth is slowed. For $\alpha = 0.049$ (light solid) the initial condition is unaffected outside the boundary. The heavy line is a classical simulation for the δ-kicked rotor. The vertical scale is logarithmic and in arbitrary units.

This situation occurs when $vt_{\text{p}} = \frac{1}{2}\lambda$, and hence an estimate for the boundary location is

$$p/2\hbar k_{\text{L}} = M\lambda^2/8\pi\hbar t_{\text{p}}. \tag{5}$$

Notice that this expression corresponds to the first zero-crossing of (4). The larger mass and longer optical wavelength of cesium provide a 12-fold increase over sodium in the momentum boundary location for a given pulse width.

3. Experiment

The experimental setup (Fig. 4) is similar to that of our earlier sodium-based quantum chaos experiments [19]. The experiments are performed on laser-cooled cesium atoms in a magneto-optic trap (MOT) [26,27].

The atoms are trapped in a stainless steel UHV chamber, in contrast to the earlier experiments in our group that used a quartz interaction chamber. All optical viewports are anti-reflection coated on both sides

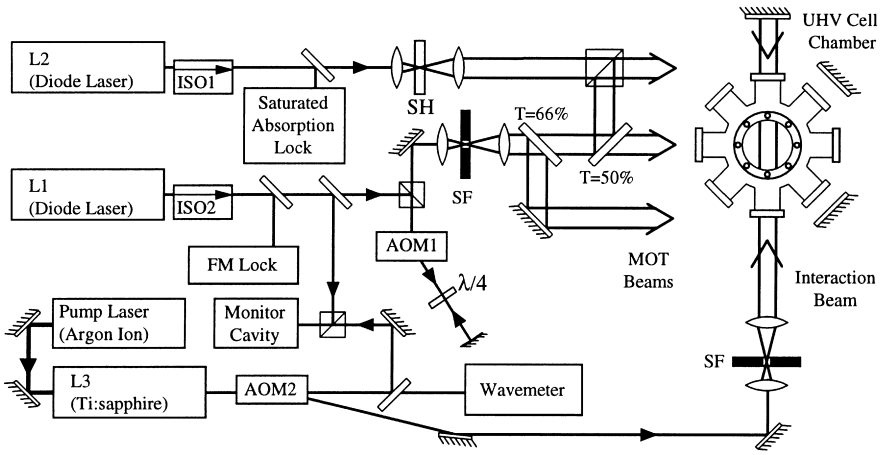

Fig. 4. Schematic diagram of the experimental setup. Two diode lasers provide the light for the MOT, and a Ti : sapphire laser provides the far-detuned standing wave.

to reduce intensity fringes on the laser beams. An ampule containing cesium metal is attached to the chamber through a valve that is opened occasionally to leak cesium vapor into the chamber. The valve is necessary because of the rather high room temperature vapor pressure of cesium. A pair of anti-Helmholtz coils surrounding the chamber provides a magnetic field gradient of 11 G/cm for the MOT. When the current to the anti-Helmholtz coils is switched off, the magnetic fields decay exponentially after a brief transient, with a 1/e time of about 3 ms. This decay time is longer than in the earlier sodium-based experiments because of induced currents in the metal chamber.

Two single-mode diode lasers (L1, L2) at 852 nm provide the light for cooling, trapping, and detection of the cesium atoms. L1 is a 100 mW distributed Bragg reflector (DBR) diode laser locked via frequency-modulation (FM) saturated-absorption spectroscopy to the $(6S_{1/2}, F = 4) \rightarrow (6P_{3/2}, F' = 4, 5)$ crossover resonance. The main beam from L1 is double-passed through a tunable acousto-optic modulator (AOM1) centered at 80 MHz that provides fast control over the intensity and detuning of the beam. During the trapping stage of the experiment, the light from L1 is tuned 15 MHz to the red of the $(6S_{1/2}, F = 4) \rightarrow (6P_{3/2}, F' = 5)$ cycling transition. The light from L1 passes through a spatial filter (SF), is collimated with a waist of 1.4 cm, and has a typical power of 23 mW at the chamber. The beam is divided into three beams of equal intensity by two beamsplitters with transmissions of 66% and 50%. The three beams are retroreflected through the center of the chamber in a standard six-beam MOT configuration.

The repump laser, L2, is a 150 mW Littrow cavity grating-stabilized diode laser. This beam is used to prevent optical pumping into the $F = 3$ ground state during the trapping and detection stages. This laser is electronically locked to the center of the $(6S_{1/2}, F = 3) \rightarrow (6P_{3/2}, F' = 4)$ saturated-absorption resonance. The beam has a typical power of 27 mW at the chamber and a waist of 7.5 mm. The intensity is controlled by a mechanical shutter (SH) with a rise/fall time of 1 ms. The beam is combined with the vertical arm of the light from L1 via a polarizing cube beamsplitter and retro-reflected through the chamber. Optical isolators (ISO1, ISO2) are used to minimize optical feedback to L1 and L2.

The entire experimental timing and data acquisition sequences are computer controlled. The timing diagram for the experiment is given in Fig. 5. After trapping and initial cooling, the intensity of L1 is reduced for 1 ms and the detuning is increased to 39 MHz to further cool the sample. Typically, we trap 10^6 atoms from the background vapor. The momentum distribution of the atoms is nearly Gaussian, although the tails of the distribution are more populated than in a

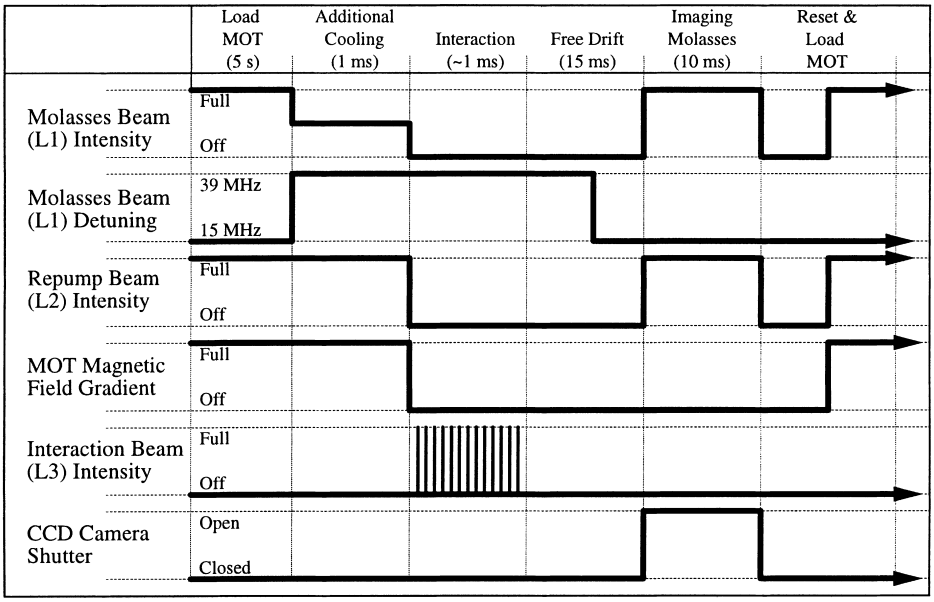

Fig. 5. An idealized timing diagram for the experiment.

purely Gaussian distribution. The center of the distribution typically fits well to a Gaussian distribution with $\sigma_p/2\hbar k_L = 4.4$, and 96% of the atoms are contained in this Gaussian. The position distribution of the atoms is also Gaussian, with $\sigma_x = 0.1$ mm.

After the final cooling, the trapping fields are turned off, leaving the momentum distribution unchanged, and the interaction potential pulses are then turned on. A stabilized single-mode Ti : sapphire laser (L3) pumped by an argon-ion laser provides the pulsed standing wave. The light from L3 passes through a fixed-frequency 80 MHz acousto-optic modulator (AOM2) that controls the pulse sequence. The beam is spatially filtered, centered on the atoms, and retro-reflected through the chamber to form a standing wave. The beam has a typical power of 290 mW at the chamber and a waist of 1.44 mm. The absolute wavelength of L3 is measured with a scanning Michelson interferometer wavemeter. A scanning confocal Fabry–Perot cavity with a 1.5 GHz free spectral range is used to monitor long-term drift of L3 during measurements.

For all the experiments described here we detuned this beam 6.1 GHz to the red of the cycling transition, with typical fluctuations of about 100 MHz. The pulse sequence consisted of a series of fixed-length pulses with a rise/fall time of 75 ns and less than 3 ns variation in the pulse duration. Sequences using pulse widths between 283 and 1975 ns (full width at half maximum) were used in these experiments to demonstrate the role of the momentum boundary. The period was 20 μs with less than 4 ns variation per pulse period as measured with a fast photodiode. The probability of spontaneous scattering was less than 0.5% per kick period for all of the parameters used. The phase noise of the standing wave due to vibrations in the optical system resulted in less than 8% of a standing wave period phase drift after 200 kicks, with a typical fluctuation timescale of 0.5 ms.

The detection of momentum is accomplished by a time-of-flight method. The atoms drift in the dark for a controlled duration, typically 15 ms. The trapping beams are then turned on in zero magnetic field, forming an optical molasses [26] that freezes the position of the atoms. The final spatial distribution is recorded via fluorescence imaging in a short (10 ms) exposure on a cooled charge-coupled device (CCD) camera. The final distribution and the free-drift time enable the determination of the momentum distribution. The maximum momentum that we can measure is

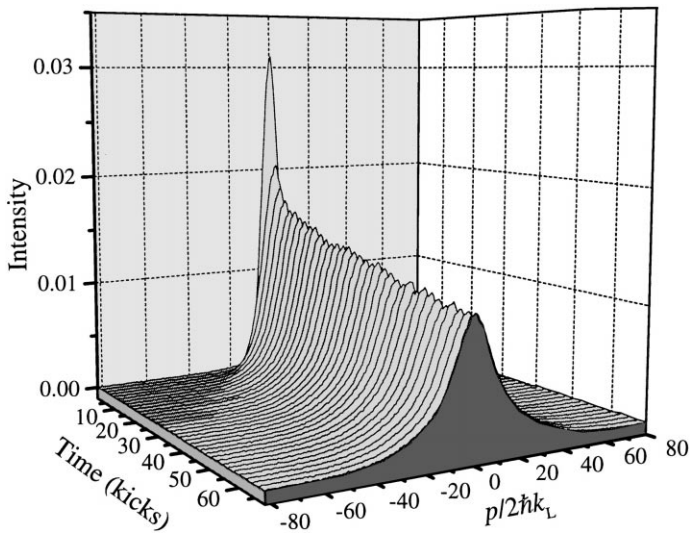

Fig. 6. Time evolution of a typical kicked-rotor experiment for $K = 11.5 \pm 10\%$, $T = 20\,\mu$s, $0.283\,\mu$s pulse width, and $\bar{\kappa} = 2.08$. The initial distribution is nearly Gaussian with $\sigma_p/2\hbar k_L = 4.4$. The final distribution is exponential with a localization length of 13. Note that the vertical axis is linear and in arbitrary units, and the time increment between distributions is 2 kicks.

limited by the size of the CCD. For a 15 ms drift time, we can detect momenta within $|p/2\hbar k_L| \approx 80$. Using shorter drift times, we could measure larger momenta at the expense of resolution. The initial spatial distribution is not deconvolved from the final momentum distributions, because the effect on the RMS width of our final distributions is on the order of 1%.

The pulse period was $T = 20\,\mu$s, corresponding to $\bar{\kappa} = 2.08$. The kick strength k was chosen to provide the best exponentially localized momentum distributions. For the shortest pulses, we used $V_0/h = 3.55$ MHz, yielding a classical stochasticity parameter of $K = 13.1$. For the longest pulses we used $V_0/h = 0.94$ MHz, corresponding to $K = 24$. The absolute uncertainty in K is $\pm 10\%$, and the largest contributions are due to the measurement of beam profile and the absolute laser power calibration.

The momentum boundary due to the nonzero pulse width is $|p/2\hbar k_L| = 213$ for our typical operating parameters. This value is a factor of four larger than in our earlier sodium experiments. The corresponding reduction in the effective value of K is only 6% out to $|p/2\hbar k_L| = 40$ and 25% at our maximum detectable momentum of $|p/2\hbar k_L| \approx 80$.

We can also estimate the effects of collisions from the experimental work of Dalibard and coworkers [28], who measured a collision cross-section of $5 \times 10^{-11}\,\mathrm{cm}^2$ for cesium atoms prepared in the $F = 4$, $m_F = 4$ ground sublevel with a temperature of $5\,\mu$K. In our initial distribution, the density is about $10^{11}\,\mathrm{cm}^{-3}$, and the mean velocity is 5 cm/s. These figures lead to a collision probability of only 2.5% in 1 ms, or 0.05% per kick period. This result actually overestimates the collision probability because our atoms are distributed among the various m_F sublevels, and so the actual collision cross-section is smaller than the figure used here.

4. Data and results

The results presented here illustrate the capabilities of the cesium setup. We observe dynamical localization and study experimentally the effects of nonzero pulse width on the kicked-rotor system. The resulting momentum distributions are compared with classical simulations. We will present a detailed study of the dependence of quantum localization on the stochasticity parameter K in a future publication.

Fig. 6 shows the time evolution for a typical kicked-rotor experiment, from the initial distribution through 68 kicks. The momentum distribution starts

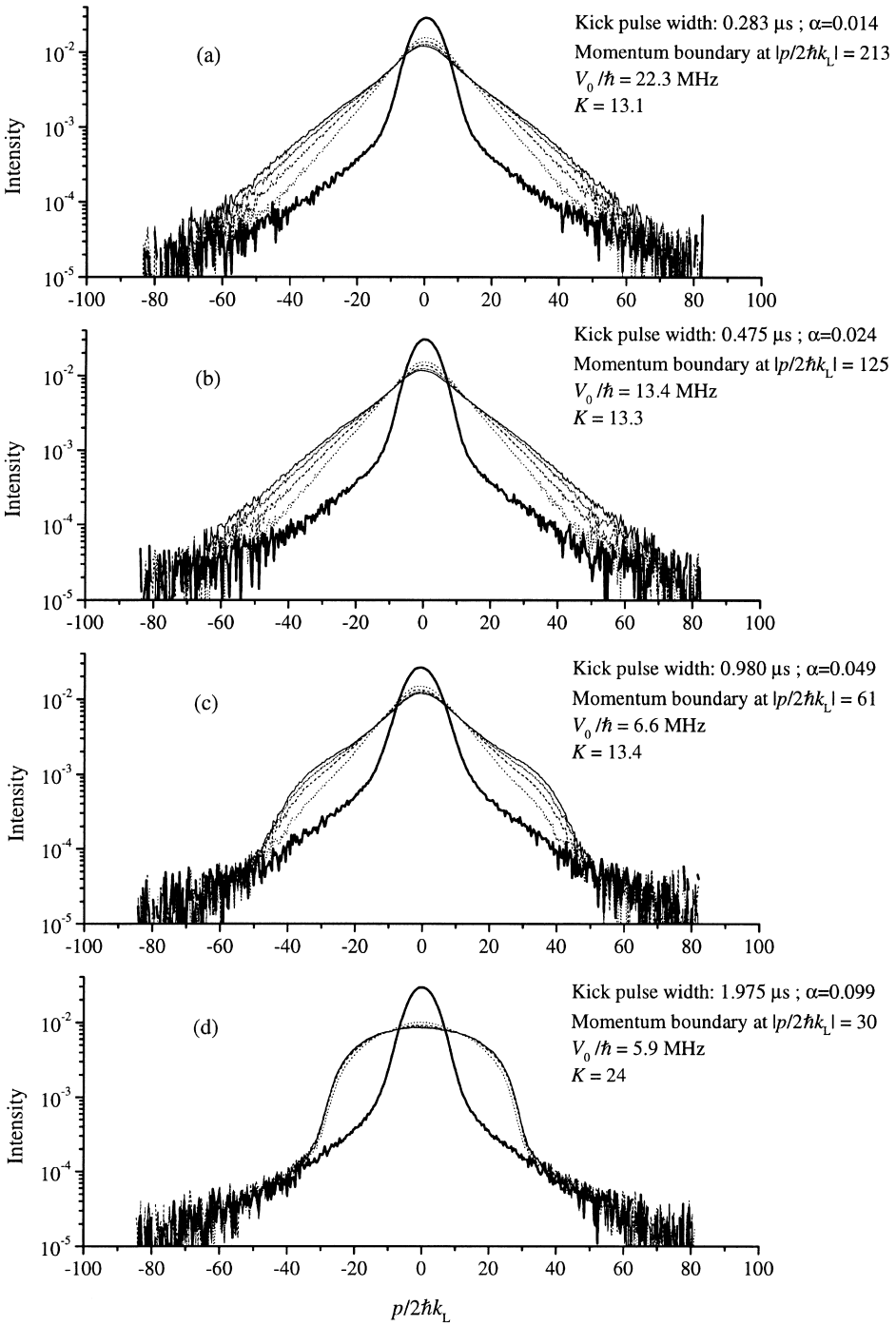

Fig. 7. Comparison of momentum distribution evolution for four different kick pulse widths from 0.3 to 2 μs. Distributions for five different times are shown on each graph: 0 kicks (heavy solid line), 17 kicks (dotted), 34 kicks (dashed), 51 kicks (dash–dot), and 62 kicks (solid). These data show the effect of the boundary on the evolution of the momentum distribution. The vertical scales are logarithmic and in arbitrary units.

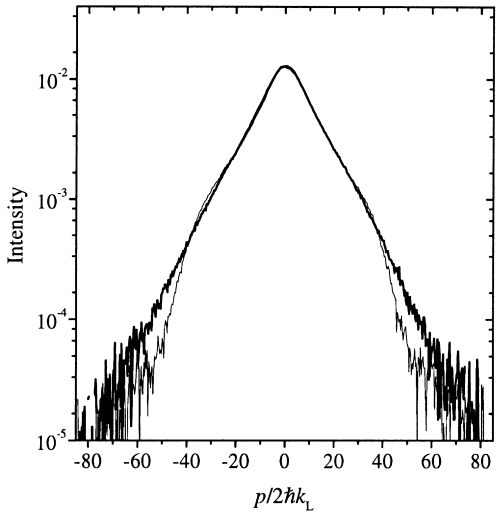

Fig. 8. Comparison of experimental momentum distributions after 51 kicks for two different pulse widths, $\alpha = 0.014$ (heavy line) and $\alpha = 0.049$ (thin line). In the $\alpha = 0.014$ case, also shown in Fig. 7(a), the boundary is at $|p/2\hbar k_L| = 213$. This boundary width is much larger than the width of the distribution, and hence the boundary does not significantly affect the exponential distribution. In the $\alpha = 0.049$ case, also shown in Fig. 7(c), the boundary is located at $|p/2\hbar k_L| = 61$. This boundary width is clearly inside the base of the exponential distribution; the momentum distribution is now distorted in its wings, while the shape at the center is nearly identical to the first case. Note that the vertical scale is logarithmic and in arbitrary units.

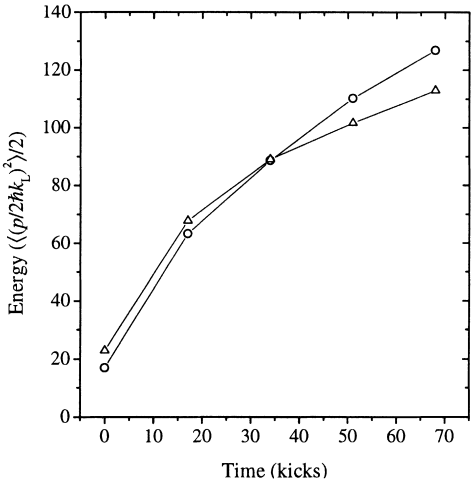

Fig. 9. Growth of energy with time for the cases in Fig. 8. The momentum boundaries are $|p/2\hbar k_L| = 213$ for the case $\alpha = 0.014$ (circles) and $|p/2\hbar k_L| = 61$ for the case $\alpha = 0.049$ (triangles). Note that the initial growth rate is the same until the distributions diffuse out to larger momenta where K_{eff} begins to drop sharply.

out with a Gaussian profile, which makes a rapid transition to a broader, exponential distribution. We observe a continued slow growth in the momentum distribution until the end of the experiment, with the distributions remaining exponential. Fig. 7(a) shows five momentum distributions for an experiment with similar parameters, taken at increments of 17 kicks. Note that the distribution remains exponential over the nearly three orders of magnitude in intensity that are resolvable in our experiment. The slow growth of the localized distribution is also evident in this figure.

Fig. 7 compares experiments using four different pulse widths with the corresponding momentum boundaries as predicted by Eq. (5). In the first case, Fig. 7(a), the boundary of $|p/2\hbar k_L| = 213$ is three times larger than the $|p/2\hbar k_L| = 70$ resolvable width of our distribution. This situation is ideal for experimental studies of the quantum kicked rotor, since the momentum distribution remains well within the boundary. In Fig. 7(b), we see that although the distance between the boundaries at $|p/2\hbar k_L| = 125$ is less than twice the width of the final distribution, there is little effect on the shapes of the distributions. In Fig. 7(c), the boundary is located at $|p/2\hbar k_L| = 61$, and it has a clear effect on the wings of the distributions. Notice, however, that after 17 kicks the distribution still looks exponential. Fig. 7(d) shows a case where the boundary at $|p/2\hbar k_L| = 30$ is well within the exponential distributions shown in Fig. 7(a). In this case, the distribution quickly reaches the boundary, and the diffusion process halts before quantum localization sets in. It is also interesting to note that the portions of the initial distributions that are outside the boundary in Figs. 7(c) and (d) remain stationary. This behavior is a result of the presence of the invariant curves past the boundary, as shown in Fig. 2, that strongly inhibit momentum transport. These observations are consistent with a previous theoretical study of the kicked rotor with finite pulses [29].

The dynamics near the center of the distribution appear to be relatively insensitive to the location of the boundary. Fig. 8 compares the distributions after 51

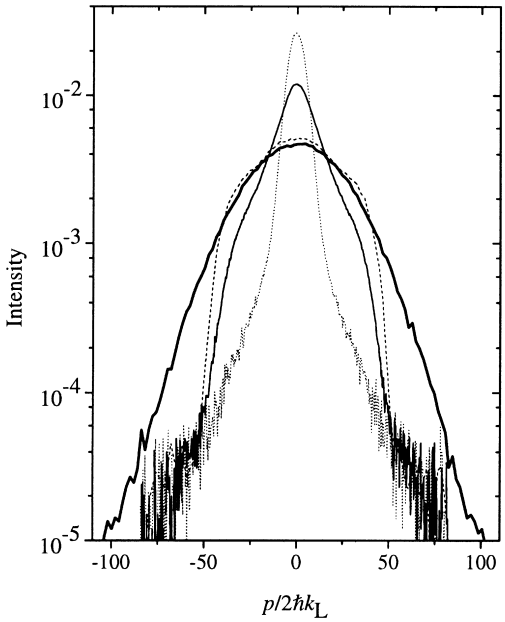

Fig. 10. Comparison of experimental momentum distributions after 68 kicks to the classical simulations of Fig. 3. Both square-pulse cases, the experiment (light solid line) and the simulation (dashed line), have the same pulse width $\alpha = 0.049$ and hence the same boundary, although K is slightly different between the two cases ($K = 11.1$ and 10.5, respectively). The experimental data clearly manifests its quantum nature through a characteristic exponential profile in the central region. The classical square-pulse simulation instead matches the classical δ-kicked rotor simulation (heavy solid line) in the central region. The initial distribution (dotted line) remains unchanged outside the boundary. Note that the vertical scale is logarithmic and in arbitrary units.

kicks from Figs. 7(a) and (c). It is clear that the portion of the distribution in the central region remains unaffected by the boundary, but there is substantial deviation between the two cases in the wings of the distributions. Fig. 9 shows that the initial energy growth rate is the same for the two boundary locations in Fig. 8. It is only as the distribution nears the boundary that further growth is inhibited. This point is significant because much of the theoretical analysis of this system has been done using the long-term diffusion in energy, which is especially sensitive to the high-momentum tails of the distribution.

In Fig. 10 we compare the intermediate case of Fig. 7(c) ($\alpha = 0.049$) to the classical simulation shown in Fig. 3. The distributions shown correspond to 68 kicks. There are several important features in this comparison. First, the classical square-pulse case follows the δ-kick case out to the boundary. Second, the experimental distribution is characteristically exponential near its center, and then it drops off at the boundary as in the classical simulation. Finally, the initial conditions in both the classical simulation and the experiment remain unchanged outside the boundary. Therefore, in the central region, both the classical simulation and the experiment behave as they would in the limit of δ-kicks, displaying classical diffusion and quantum localization, respectively. Their behavior in the boundary region, however, is quite similar.

5. Future directions

So far, we have considered the observation of dynamical localization and the role of the boundary in our experiment. We will now discuss experiments that are currently under development in our laboratory that extend these results. Specifically, we will consider two classes of experiments: noise and dissipation in the quantum kicked rotor and the probing of local phase space structure using localized initial states.

The study of noise and dissipation is of great importance in many areas of physics. In particular, the role of noise and dissipation in quantum mechanics has generated much theoretical interest in recent years, especially in the context of classically chaotic systems. In the case of the quantum kicked rotor, noise and dissipation are expected to lead to destruction of quantum localization. This *delocalization* phenomenon is the prototype for demonstrating the important role of noise in recovering the (chaotic) classical limit from its quantum description [22–24,30]. The kicked rotor is also an interesting setting for the study of noise and dissipation, because of its fundamental importance in quantum chaos.

The noise-induced delocalization experiments are relatively straightforward generalizations of the dynamical localization experiments. To introduce noise in the experiment, one simply adds a random, time-dependent perturbation to one of the system parameters. Suitable parameters include the kick strength, the time between kicks, or the phase of the standing-wave

potential. Alternatively, one may introduce dissipation by coupling the atoms to a heat reservoir; this coupling can be accomplished by allowing the atoms to undergo spontaneous emission events, by either tuning the standing-wave light close to resonance or introducing weak, near-resonant light from the trapping beams. The predicted behavior of the quantum kicked rotor in the presence of noise [8,22,24] is that instead of localizing after the quantum break time, the momentum distribution will continue to diffuse at a reduced rate D_q, where the magnitude of D_q increases with the noise amplitude. Delocalization due to amplitude noise was seen in the previous sodium-based experiments, but the momentum boundary prevented a quantitative study of the effect [31].

We will also implement a method for preparing localized initial conditions, so that we can study local structures in the classical phase space. Our current initial conditions are completely delocalized in position over the scale of one period of the standing wave. These initial conditions are a serious limitation for studies of mixed phase space, because the resulting dynamics are an average over many structures contained within the initial distribution. If we were able to produce initial states that were narrow in both position and momentum, we could study many interesting effects, including local fluctuations in the localization length, phase-space scarring, tunneling between islands of stability, and transport across KAM tori.

In order to prepare localized initial states, we must first prepare a distribution that is further localized in momentum. We will accomplish this task via a stimulated Raman "tagging" approach [32]. This approach takes advantage of the fact that the cesium D_2 line has a ground state that is split into two hyperfine levels, $F = 3$ and $F = 4$, separated by $\sim 9.2\,\mathrm{GHz}$. It is possible to induce two-photon stimulated Raman transitions between the two ground levels by illuminating the atoms with two laser fields that are each detuned several GHz from the D_2 line, but have a relative frequency offset that is near the ground state splitting. Because the fields are far-detuned, this process is coherent. If the two fields are counterpropagating, the interaction will be sensitive to Doppler shifts, and the resonance condition is

$$\nu_2 - \nu_1 = 9.2\,\mathrm{GHz} - \frac{v}{c}(\nu_1 + \nu_2), \tag{6}$$

where ν_1 and ν_2 are the frequencies of the two fields, v the velocity of the atom, and c is the speed of light. The experimental sequence begins by cooling and trapping atoms in the MOT. The repump light is then turned off, and the atoms are optically pumped into the $F = 3$ ground level. Then the trapping beams are turned off, and the stimulated Raman fields are pulsed on. The relative detunings of the Raman beams are chosen so that the atoms promoted to the $F = 4$ ground state are near $p = 0$ after the Raman pulse. The width of the momentum distribution of these "tagged" atoms is set mainly by the duration of the pulse. Once the coldest atoms have been tagged, the experiment can proceed as usual. At the end of the experiment, we turn on the freezing molasses without the repump light in order to illuminate and image only those atoms that were tagged. The untagged atoms effectively drop out of the experiment, leaving behind a smaller atomic sample with a narrower initial momentum distribution.

We now consider localization in position. We first prepare the atoms using the stimulated Raman technique such that the momentum distribution is within the interval $(-\hbar k_L, +\hbar k_L)$. The standing-wave potential is then turned on adiabatically. Under these conditions, all the atoms are loaded into the lowest energy band of the periodic potential [33]. As the depth of the potential is increased, the atoms become localized near the bottoms of the potential wells, at the expense of increased temperature. In the limit of deep potential wells, the lowest energy band approximates the ground state of the harmonic oscillator, since the well bottoms are locally parabolic; hence, in this limit, the prepared states are in principle minimum uncertainty Gaussian wave packets, modulo 2π in position. The aspect ratio of the distribution in phase space can be controlled via the final well depth.

The prepared initial distribution that we have described so far is localized about $x = p = 0$. It is useful to have techniques for centering the distribution at other points of interest in phase space. A shift in the position of the distribution can be accom-

plished by suddenly shifting the phase of the standing wave at the beginning of the experiment. Such a phase shift can, for example, be accomplished by placing an electro-optic modulator in the path of one of the two beams that form the standing-wave potential. A shift in the momentum of the distribution can be achieved by introducing a relative frequency shift between the two standing-wave beams, producing a standing wave moving at a velocity proportional to the shift.

6. Summary

We have constructed a quantum chaos experiment in cesium that models the δ-kicked rotor. This apparatus is capable of a much wider range of experiments than the sodium-based experiments. The primary advantage of this new experiment lies in the physical characteristics of cesium, which reduce the effects of the momentum boundary and bring the experiment closer to the δ-kick limit. We will soon extend the capabilities of this experiment to study the effects of noise and decoherence on localization and to study structures in mixed phase space.

Acknowledgements

This work was supported by the Robert A. Welch Foundation and the National Science Foundation. DAS acknowledges support from a National Science Foundation Graduate Research Fellowship.

References

[1] G. Casati, B.V. Chirikov, J. Ford, F.M. Izrailev, in: G. Casati, J. Ford (Eds.), Stochastic Behaviour in Classical and Quantum Hamiltonian Systems, Lecture Notes in Physics, vol. 93, Springer, Berlin, 1979.
[2] B. Chirikov, F.M. Izrailev, D.L. Shepelyansky, Sov. Sci. Rev. C 2 (1981) 209.
[3] S. Fishman, D.R. Grempel, R.E. Prange, Phys. Rev. Lett. 49 (1982) 509.
[4] D.R. Grempel, R.E. Prange, S. Fishman, Phys. Rev. A 29 (1984) 1639.
[5] D.L. Shepelyansky, Physica D 8 (1982) 208.
[6] D.L. Shepelyansky, Phys. Rev. Lett. 56 (1986) 677.
[7] D.L. Shepelyansky, Physica D 28 (1987) 103.
[8] D. Cohen, Phys. Rev. A 44 (1991) 2292.
[9] R. Blümel, W.P. Reinhardt, Chaos in Atomic Physics, Cambridge, 1997.
[10] J.E. Bayfield, P.M. Koch, Phys. Rev. Lett. 33 (1974) 258.
[11] E.J. Galvez, B.E. Sauer, L. Moorman, P.M. Koch, D. Richards, Phys. Rev. Lett. 61 (1988) 2011.
[12] J.E. Bayfield, G. Casati, I. Guarneri, D.W. Sokol, Phys. Rev. Lett. 63 (1989) 364.
[13] R. Blümel, R. Graham, L. Sirko, U. Smilansky, H. Walther, K. Yamada, Phys. Rev. Lett. 62 (1989) 341.
[14] L.E. Reichl, The Transition to Chaos in Conservative Classical Systems: Quantum Manifestations, Springer-Verlag, Berlin, 1992.
[15] R. Graham, M. Schlautmann, D.L. Shepelyansky, Phys. Rev. Lett. 67 (1991) 255.
[16] R. Graham, M. Schlautmann, P. Zoller, Phys. Rev. A 45 (1992) R19.
[17] F.L. Moore, J.C. Robinson, C. Bharucha, P.E. Williams, M.G. Raizen, Phys. Rev. Lett. 73 (1994) 2974.
[18] J.C. Robinson, C. Bharucha, F.L. Moore, R. Jahnke, G.A. Georgakis, Q. Niu, M.G. Raizen, B. Sundaram, Phys. Rev. Lett. 74 (1995) 3963.
[19] F.L. Moore, J.C. Robinson, C.F. Bharucha, B. Sundaram, M.G. Raizen, Phys. Rev. Lett. 75 (1995) 4598.
[20] J.C. Robinson, C.F. Bharucha, K.W. Madison, F.L. Moore, B. Sundaram, S.R. Wilkinson, M.G. Raizen, Phys. Rev. Lett. 76 (1996) 3304.
[21] G.P. Collins, Phys. Today 48 (1995) 18.
[22] E. Ott, T.M. Antonsen Jr., J.D. Hanson, Phys. Rev. Lett. 53 (1984) 2187.
[23] T. Dittrich, R. Graham, Europhys. Lett. 4 (1987) 263.
[24] S. Fishman, D.L. Shepelyansky, Europhys. Lett. 16 (1991) 643.
[25] G. Casati, I. Guarneri, D.L. Shepelyansky, Phys. Rev. Lett. 62 (1989) 345.
[26] S. Chu, Science 253 (1991) 861.
[27] C. Cohen-Tannoudji, in: J. Dalibard, J.M. Raimond, J. Zinn-Justin (Eds.), Fundamental Systems in Quantum Optics, Les Houches, 1990, Elsevier, London, 1992.
[28] M. Arndt, M. Ben Dahan, D. Guéry-Odelin, M.W. Reynolds, J. Dalibard, Phys. Rev. Lett. 79 (1997) 625.
[29] R. Blümel, S. Fishman, U. Smilansky, J. Chem. Phys. 84 (1986) 2604.
[30] W.H. Zurek, J.P. Paz, Phys. Rev. Lett. 72 (1994) 2508.
[31] J.C. Robinson, Ph.D. Dissertation, The University of Texas at Austin, 1995.
[32] M. Kasevich, D. Weiss, E. Riis, K. Moler, S. Kasapi, S. Chu, Phys. Rev. Lett. 66 (1991) 2297.
[33] M. Raizen, C. Salomon, Q. Niu, Phys. Today (1997) 30.